An Imaging and Measurement System for Robust Reconstruction of Weld Pool During Arc Welding

Zhenzhou Wang

***Abstract*—Robust measurement of the specular weld pool surface can help better understand the complex welding processes and provide feedback for robotic welding. The strong arc light and the specular surface of the weld pool make it difficult for the direct sensing measurement. In this paper, a novel imaging and measurement system is proposed, and it makes use of the strong penetrability of the laser to avoid the interference of arc light and obtain the surface information of the weld pool. By intercepting the reflection of a projected laser pattern twice, the proposed system gives a closed-form solution for each reflected ray and a closed-form solution for the corresponding point on the weld pool surface. The weld pool surface can be thus reconstructed by one-shot structured light projection. To increase the robustness of the measurement system, the least deformation principle is proposed to rectify the coefficient errors of the computed plane equation. Finally, a sequence of 3-D weld pools is reconstructed and compared with state-of-art literature. The comparison verifies that our method is significantly better than all the other methods in measuring the 3-D weld pool shapes.**

***Index Terms*—Closed-form solution, dynamic, measurement, one-shot reconstruction, weld pool.**

I. Introduction

THE arc welding plays an important role in manufacturing industry and has been studied intensively for decades to achieve better quality and high productivity [1]–[3]. Sensory methods [4], [5] had been adopted for feedback control in 1980s. Seam tracking [6] is the earliest application of vision-based sensory methods in arc welding. Later, researchers [7]–[10] tried to control the welding process with more complex and accurate visual sensory information, i.e., the weld pool geometry.

Due to the importance of the weld pool shape for the penetration of arc welding, a lot of studies have been devoted to measuring the miniature weld pool just as in microfabrication and electronic packaging industry [11]–[13]. We divide the state-of-art literature of weld pool measurement methods into two categories: 1) the one-single-view-based method [14]–[22]; and 2) the stereo method [25]–[28]. For the one-single-view method, a camera is used to acquire one view, and then the view is combined with other information, e.g., phase/depth from grates in [14], thermal emissions in [16], and structured laser pattern and reflection law in [17] and [22]–[24], to achieve a better result. For the stereo method, two views are acquired by two cameras or one camera with one biprism. Its work principle is approximately the same as the traditional stereo method [29], [30].

Since it is already a common sense that the stereo method lacks robustness because of the registration problem of finding correspondences in two images, structured light methods might be a better choice for robust measurement of the 3-D shape of weld pool. However, the famous phase-measurement methods [31], [32] need multiple projections to solve the phase ambiguity, whereas the weld pool is dynamic; consequently, it is impossible to capture multiple distorted patterns for the same shape. The shape from the shading method [33] fails in solving the ambiguity between surface normal and depth. The time-of-flight methods [34], [35] are not suitable for this measurement task either. Thus, a more sophisticated method is required for the robust measurement of the weld pool geometry.

Based on the past research [36], [37], we developed a novel imaging and measurement system that comprises a laser pattern generator; two diffusive planes coupled with two cameras, respectively; one beam splitter; and a virtual camera [39], [40]. The equation of the diffusive plane is computed with one real camera and the virtual camera. The 3-D coordinates of the interception points of the laser rays on the diffusive plane are thus computed with the 2-D coordinates from the real camera and the known equation. Two points are obtained from two diffusive planes for each reflected ray; thus, the ray is determined in the world coordinate system. With known incident (projected by the laser generator) laser rays, the intersection points on the specular weld pool can be computed with a closed-form solution. The shape of the weld pool can be calculated by polynomial interpolation due to its smoothness.

The developed system is deliberately designed to overcome four challenges inherent in weld pool measurement. First, the ambient strong arc light makes the direct sensing of the weld pool difficult, and it also fails the pico laser projector used in [36], [37]. To avoid direct sensing, we project a pattern of laser rays onto the weld pool and then obtain the surface

Manuscript received March 9, 2014; revised September 17, 2014 and January 9, 2015; accepted February 5, 2015. Date of publication February 19, 2015; date of current version June 26, 2015. This work was supported by the University of Kentucky under Grant CMMI-0927707.

The author is with the State Key Laboratory of Robotics at Shenyang Institute of Automation, Chinese Academy of Sciences, Shenyang 110016, China (e-mail: zzwangsia@yahoo.com).

Color versions of one or more of the figures in this paper are available online at http://ieeexplore.ieee.org.

Digital Object Identifier 10.1109/TIE.2015.2405494

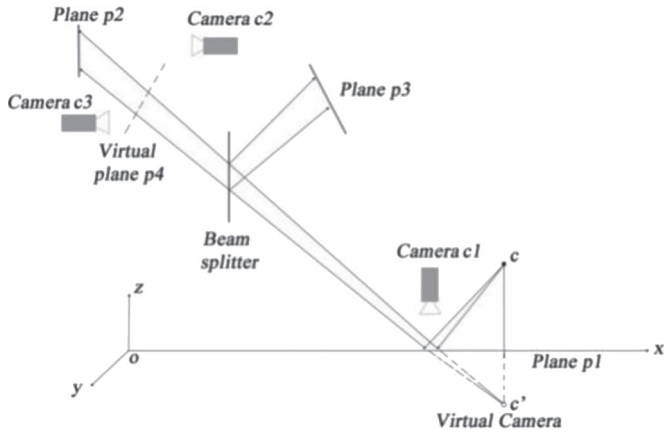

Fig. 1. Working principle of the proposed system.

information from the reflected patterns imaged on the two diffusive planes. However, the use of the SNF laser [38] brought the imperfect central projection of laser rays that in turn caused great distortion and coefficient errors, which is analyzed in this paper to fill in the gap of [38]. The least deformation principle is then proposed to rectify the coefficient errors. Second, the weld pool is miniature (typically $3 \times 3 \times 0.5$ mm^3), which requires powerful camera lens and a sophisticated imaging and measurement system with excellent noise resistance performance to be installed on the enormous welding system. Third, the laser has the out-of-focus problem. Thus, distances to place the imaging planes need to be selected carefully by considering both the arc light effect and laser focus. Fourth, the weld pool is dynamic, which makes traditional structured light methods using multiple scans of the same static surface fail. To achieve one shot reconstruction, the developed system computes the intersection points of the projected rays and their reflected rays with closed-form solutions.

This paper is organized as follows. Section II describes the working principle of the proposed imaging and measurement system. Analysis of the system error is given, and the least deformation principle is proposed in Section III. The experimental system is described in Section IV, and experimental results are shown and discussed in Section V. In Section VI, conclusion is drawn, and the future work is discussed.

II. Working Principle of the Proposed System

The working principle of the proposed imaging and measurement system [36] is shown in Fig. 1. There are three planes, i.e., $p1$, $p2$, and $p3$, with three cameras, i.e., $c1$, $c2$, and $c3$, aimed at them, respectively. The projection center of the projector is denoted C, and the projection center of the virtual camera is denoted C'. Plane $p1$ is defined as the reference plane $z = 0$, and it originates at O. During calibration, the equations of the two diffusive planes $p2$ and $p4$ are computed. During reconstruction, laser rays projected onto and reflected by plane $p1$ are traced by cameras $c2$ and $c3$ with a beam splitter to intercept one ray by two points on planes $p2$ and $p4$, respectively. The closed-form solution can be then obtained by calculating the intersections of the incident and the traced rays.

A. Plane Equations

The equation of the reference plane $p1$ is known as $z = 0$, which can be written as $\pi_1 = [\mathbf{0}, \mathbf{0}, \mathbf{1}, \mathbf{0}]^T$. The equation π_2 of $p2$ is then computed as follows:

$$\pi_2 = \left(P^T\right)^{-1} \pi_1 \tag{1}$$

$$P = \begin{bmatrix} 1 & 0 & 0 & -C_x \\ 0 & 1 & 0 & -C_y \\ 0 & 0 & 1 & f \\ 0 & 0 & 0 & 1 \end{bmatrix} \begin{bmatrix} r_0 & r_1 & r_2 & T_X \\ r_3 & r_4 & r_5 & T_Y \\ r_6 & r_7 & r_8 & T_Z \\ 0 & 0 & 0 & 1 \end{bmatrix} \tag{2}$$

where (C_x, C_y) and f are the principle points and focal length of the virtual camera, respectively. The mirror plane $p1$ is treated as the image plane of the virtual camera. The rotation matrix $R = [r1, r2, r3]$ and translation vector $T = [T_X, T_Y, T_Z]^T$ defines the affine between $p1$ and $p2$, and they need to be computed by the following [41]:

$$r1 = [r_0, r_3, r_6]^T = \frac{K^{-1}h_1}{||K^{-1}h_1||} \tag{3}$$

$$r2 = [r_1, r_4, r_7]^T = \frac{K^{-1}h_2}{||K^{-1}h_1||} \tag{4}$$

$$T = [T_X, T_Y, T_Z]^T = \frac{K^{-1}h_3}{||K^{-1}h_1||} \tag{5}$$

$$r3 = [r_2, r_5, r_8]^T = r1 \times r2 \tag{6}$$

where $H = [h_1, h_2, h_3,]$ is the homography between the plane $p2$ and the virtual camera image plane $p1$. K is the intrinsic matrix of the virtual camera and is defined as

$$K = \begin{bmatrix} f & 0 & C_x \\ 0 & f & C_y \\ 0 & 0 & 1 \end{bmatrix}. \tag{7}$$

To compute H, we need to obtain two sets of coordinates (x_i, y_i) and $(X_i, Y_i) i = 1, \ldots, N$ from $p1$ and $p2$, respectively, by camera calibration. Then, H can be computed by the following:

$$x_i = \frac{H_{11}X_i + H_{12}Y_i + H_{13}}{H_{31}X_i + H_{32}Y_i + H_{33}}, \quad i = 1, \ldots, N \tag{8}$$

$$y_i = \frac{H_{21}X_i + H_{22}Y_i + H_{23}}{H_{31}X_i + H_{32}Y_i + H_{33}}, \quad i = 1, \ldots, N \tag{9}$$

$$H = \begin{bmatrix} H_{11} & H_{22} & H_{13} \\ H_{21} & H_{22} & H_{23} \\ H_{31} & H_{32} & H_{33} \end{bmatrix} \tag{10}$$

where N is the number of the points chosen to compute the homography. Use N points to stack (8) and (9) into one equation, and solve it by singular value decomposition with maximum-likelihood estimation. After H is obtained, all the unknowns in (2) are obtained, and the plane equation of $p2$ is obtained. In the same way, the equation π_4 of the virtual plane $p4$ is computed.

B. Equations of Incident Rays

Each incident ray is formulated by the following:

$$\frac{x_l^i - x_0^i}{a^i} = \frac{y_l^i - y_0^i}{b^i} = \frac{z_l^i - z_0^i}{c^i} = t^i \tag{11}$$

where i denotes the index of the incident ray, and l denotes the index of the interception points on different horizontal planes. t is the continuous-time variable. a, b, and c are the line coefficients. $i = 1, \ldots, N; l = 1, \ldots, 6$.

To compute the equations of the incident rays, we replace the mirror plane $p1$ with a diffusive plane, which is also horizontal, and its original equation is also $z = 0$. By moving it downward 1 mm each time, we obtain more horizontal planes, i.e., $z = -1, z = -2, z = -3, z = -4, z = -5$. Accordingly, six interception points for each incident ray are obtained. Then, the equation of each incident laser ray (11) is determined using the singular value decomposition algorithm.

If the computed equations of the rays are exactly accurate and the used laser projector is perfectly central projection, there will be only one intersection point for all these laser rays. However, due to noise and imperfect central projection, not all these laser rays would intersect exactly at one point, and some of them may not even intersect at all. To find the projection center, the least squares algorithm is used to find the point that is the nearest to all of these laser rays.

C. Three-Dimensional Mapping

We need the mapping from the 2-D camera coordinates to the 3-D world coordinates in order to trace the rays in real time during the online weld pool measurement process. After the 3-D mapping is known, each emergent ray can be determined by the image coordinates in the two cameras $c2$ and $c3$. The world coordinates of the interception points on the diffusive planes are computed from three known elements: 1) the plane equation; 2) the known camera coordinates; and 3) the homography between the diffusive plane and camera image plane.

To determine this homography, we need two sets of points $(X_i', Y_i'), i = 1, \ldots, N$ from $p1$ and $(u_i, v_i), i = 1, \ldots, N$ from the camera image plane, respectively. To obtain $(X_i', Y_i'), i = 1, \ldots, N$, we compute the equations of the reflected laser rays first

$$L_i = [x_i, y_i, 0, 1]^T [C_x, C_y, -f, 1] - [C_x, C_y, -f, 1]^T [x_i, y_i, 0, 1]. \quad (12)$$

Then, the interception point of the reflected laser ray with the $p2$ denoted $P_i = [X_i', Y_i', Z_i', 1]^T$ can be computed as follows:

$$P_i = L_i \pi_2. \quad (13)$$

The homography H' between the coordinates $X_i', Y_i', i = 1, \ldots, N$ of the interception points on $p2$ and their camera coordinates $(u_i, v_i), i = 1, \ldots, N$ in $c2$ is computed by singular value decomposition.

With H' and $(u_i, v_i), i = 1, \ldots, N$, the world coordinates (X_i', Y_i', Z_i') of the interception points on the diffusive planes are computed as follows:

$$\begin{bmatrix} X_i' \\ Y_i' \\ 1 \end{bmatrix} = (H')^{-1} \begin{bmatrix} u_i \\ v_i \\ 1 \end{bmatrix} \quad (14)$$

$$Z_i' = \frac{\pi_2(1) X_i' + \pi_2(2) Y_i' + \pi_2(4)}{-\pi_2(3)}. \quad (15)$$

In the same way, the 3-D coordinates of the interception points on $p4$ are computed.

D. Three-Dimensional Reconstruction

After the world coordinates of the interception points on $p2$ and $p4$ are calculated, we know two points for each reflected laser ray, and the reflected laser ray is determined uniquely. The equation of the each emergent laser ray is formulated as

$$\mathrm{EL}_i = \left[X_i^2, Y_i^2, Z_i^2, 1\right]^T \left[X_i^4, Y_i^4, Z_i^4, 1\right] - \left[X_i^4, Y_i^4, Z_i^4, 1\right]^T \left[X_i^2, Y_i^2, Z_i^2, 1\right] \quad (16)$$

where (X_i^2, Y_i^2, Z_i^2) and (X_i^4, Y_i^4, Z_i^4) are the coordinates of the interception points on $p2$ and $p4$, respectively. Equation (16) is reformulated as

$$\frac{X^i - X_0^i}{A^i} = \frac{Y^i - Y_0^i}{B^i} = \frac{Z^i - Z_0^i}{C^i} = T^i \quad (17)$$

where $X_o^i = X_i^2 + X_i^4/2$, $Y_o^i = Y_i^2 + Y_i^4/2$, $Z_o^i = Z_i^2 + Z_i^4/2$, $A^i = X_i^2 - X_i^4$, $B^i = Y_i^2 - Y_i^4$, and $C^i = Z_i^2 - Z_i^4$ is the continuous-time variable.

Since the incident laser rays have already been calculated by (11), the intersection point of the incident ray with its reflected ray or the nearest point to the two rays if they do not intersect can be computed. A total number of N 3-D points of the surface can be acquired.

The distance between point (x^i, y^i, z^i) on the incident ray and the point on the reflected ray (X^i, Y^i, Z^i) is computed as follows:

$$d^i = \sqrt{(X^i - x^i)^2 + (Y^i - y^i)^2 + (Z^i - z^i)^2}. \quad (18)$$

Substituting (11) and (17) into (18), the following equation is acquired:

$$\left(d^i\right)^2 = \left(A^i T^i + X_0^i - a^i t^i - x_0^i\right)^2 + \left(B^i T^i + Y_0^i - b^i t^i - y_0^i\right)^2 + \left(C^i T^i + Z_0^i - c^i t^i - z_0^i\right)^2 \quad (19)$$

where only T^i and t^i are unknown. It is treated as the quadratic equation of T^i first. The minimum value of the quadratic equation is computed by finding the point where the derivative of the equation equals zero. Solving the derivative equation, we get

$$T^i = \rho_1 t^i + \rho_2 \quad (20)$$

where

$$\rho_1 = \frac{a^i A^i + b^i B^i + c^i C^i}{A^i A^i + B^i B^i + C^i C^i} \quad (21)$$

$$\rho_2 = \frac{A^i x_0^i + B^i y_0^i + C^i z_0^i - A^i X_0^i - B^i Y_0^i - C^i Z_0^i}{A^i A^i + B^i B^i + C^i C^i}. \quad (22)$$

Substituting (20) into (19) and setting the derivative of t^i to zero and solving it, the value of t^i is obtained:

$$t^i = \frac{\mu_1 + \mu_2 + \mu_3}{\sigma} \quad (23)$$

where

$$\sigma = \left(A^i \rho_1 - a^i\right)^2 + \left(B^i \rho_1 - b^i\right)^2 + \left(C^i \rho_1 - c^i\right)^2 \quad (24)$$

$$\mu_1 = -(A^i \rho_1 - a^i)(A^i \rho_2 + X_0^i - x_0^i) \quad (25)$$

$$\mu_2 = -(B^i \rho_1 - b^i)(B^i \rho_2 + Y_0^i - y_0^i) \quad (26)$$

$$\mu_3 = -(C^i \rho_1 - c^i)(C^i \rho_2 + Z_0^i - z_0^i). \quad (27)$$

By substituting the value of t^i back into (20), the value of T^i is obtained:

$$T^i = \rho_1 \frac{\mu_1 + \mu_2 + \mu_3}{\sigma} + \rho_2. \tag{28}$$

Substitute the value of t^i and the value of T^i into (11) and (17), respectively. Two nearest points are acquired, i.e.,

$$\begin{bmatrix} x^i \\ y^i \\ z^i \end{bmatrix} = \frac{\mu_1 + \mu_2 + \mu_3}{\sigma} \begin{bmatrix} a^i \\ b^i \\ c^i \end{bmatrix} + \begin{bmatrix} x_0^i \\ y_0^i \\ z_0^i \end{bmatrix} \tag{29}$$

$$\begin{bmatrix} X^i \\ Y^i \\ Z^i \end{bmatrix} = \left(\rho_1 \frac{\mu_1 + \mu_2 + \mu_3}{\sigma} + \rho_2 \right) \begin{bmatrix} A^i \\ B^i \\ C^i \end{bmatrix} + \begin{bmatrix} X_0^i \\ Y_0^i \\ Z_0^i \end{bmatrix}. \tag{30}$$

When the two points are not equal, the coordinate of the interception point is approximated by the following:

$$\begin{bmatrix} X_r^i \\ Y_r^i \\ Z_r^i \end{bmatrix} = \frac{1}{2} \begin{bmatrix} X^i \\ Y^i \\ Z^i \end{bmatrix} + \frac{1}{2} \begin{bmatrix} x^i \\ y^i \\ z^i \end{bmatrix}. \tag{31}$$

After all the sampled points are calculated, a mirror surface can be reconstructed by the polynomial interpolation, i.e.,

$$P_f(1:N_t) = \arg\min_f \left((1-\alpha) \times \sum_{j=1}^{N_t} |P_r([v(i)]) - f(v(i))|^2 + \alpha \times \int \left| \frac{d^2 f(t)}{dt^2} \right|^2 dt \right) \tag{32}$$

where

$$v(i) = 1 + (i-1)/M \quad i = 1:N_t, \quad N_t = M \times N \tag{33}$$

with P_r denoting the reconstructed sampled point, and P_f denoting the point after interpolation. N_t denotes the number of surface points after interpolation, and it is M times of the number of sampled points N. α is a smoothing factor.

III. System Error Analysis and Least Deformation Principle

From (15), it is seen that the z coordinate of the interception point is computed with the plane equations after its x and y coordinates are obtained from (14). Since H' is obtained from a set of points and maximum-likelihood estimation, it is insensitive to noise; thus, the computed x, y coordinates are robust. However, (15) indicates that the z coordinate is very sensitive to the plane coefficient errors.

To analyze how the reconstruction accuracy is affected by the plane coefficient errors, we suppose two parallel incident rays with the following equations are projected on $p_1(z=0)$ at $(x_0, y_0, 0)$ and $(x_0 - 1, y_0, 0)$, respectively, i.e.,

$$\frac{x - x_0}{a} = \frac{y - y_0}{b} = \frac{z}{c} = t \tag{34}$$

$$\frac{x - x_0 + 1}{a} = \frac{y - y_0}{b} = \frac{z}{c} = t. \tag{35}$$

We define the difference of these two interception points in z direction as depth difference, and it is denoted Z_d. Their reflected rays are formulated as follows:

$$\frac{X - x_0}{-a} = \frac{Y - y_0}{-b} = \frac{Z}{c} = T \tag{36}$$

$$\frac{X - x_0 + 1}{-a} = \frac{Y - y_0}{-b} = \frac{Z}{c} = T. \tag{37}$$

The first reflected ray (34) intercepts the imaging plane $p2$ at

$$X_2 = x_0 - \frac{a\left(x_0\pi_2(1) + y_0\pi_2(2) + \pi_2(4)\right)}{a\pi_2(1) + b\pi_2(2) - c\pi_2(3)} \tag{38}$$

$$Y_2 = y_0 - \frac{b\left(x_0\pi_2(1) + y_0\pi_2(2) + \pi_2(4)\right)}{a\pi_2(1) + b\pi_2(2) - c\pi_2(3)} \tag{39}$$

$$Z_2 = \frac{c\left(x_0\pi_2(1) + y_0\pi_2(2) + \pi_2(4)\right)}{a\pi_2(1) + b\pi_2(2) - c\pi_2(3)}. \tag{40}$$

Equation (38) can be written in the same format as (15), i.e.,

$$Z_2 = \frac{\pi_2(1)X_2 + \pi_2(2)Y_2 + \pi_2(4)}{-\pi_2(3)}. \tag{41}$$

In practical implementation, since X_2 and Y_2 are acquired by (14), they are less sensitive to noise compared with that acquired by(15). To facilitate our analysis, we assume X_2 and Y_2 are computed by (14) free of error. Then, they will have the same values as (38) and (39).

While the corresponding z coordinate is computed by the imperfect plane equation, i.e.,

$$Z_2^e = \frac{\pi_2^e(1)X_2 + \pi_2^e(2)Y_2 + \pi_2^e(4)}{-\pi_2^e(3)}. \tag{42}$$

Similarly, the other three interception points of the two reflected rays with $p2$ and $p4$ are obtained. Consequently, the equations of the reflected rays that are used to compute the interception points on the specular surface are changed to

$$\frac{X - x_0}{-a} = \frac{Y - y_0}{-b} = \frac{Z}{c^e} = T \tag{43}$$

$$\frac{X - x_0 + 1}{-a} = \frac{Y - y_0}{-b} = \frac{Z}{c^{e'}} = T \tag{44}$$

where

$$c^e = \frac{\pi_2^e(1)X_2 + \pi_2^e(2)Y_2 + \pi_2^e(4)}{-\pi_2^e(3)} - \frac{\pi_4^e(1)X_4 + \pi_4^e(2)Y_4 + \pi_4^e(4)}{-\pi_4^e(3)} \tag{45}$$

$$c^{e\prime} = \frac{\pi_2^e(1)X_2' + \pi_2^e(2)Y_2' + \pi_2^e(4)}{-\pi_2^e(3)} - \frac{\pi_4^e(1)X_4' + \pi_4^e(2)Y_4' + \pi_4^e(4)}{-\pi_4^e(3)} \tag{46}$$

with (X_2, Y_2), (X_4, Y_4), (X_2', Y_2'), and (X_4', Y_4') being the x and y coordinates of the four interception points of the two reflected rays with the two planes.

From the following:

$$Z_d^r = T|c^e - c^{e'}|. \tag{47}$$

TABLE I
COMPARISON OF COEFFICIENTS FOR PLANE 2

	$\pi_2(1)$	$\pi_2(2)$	$\pi_2(3)$	$\pi_2(4)$
Original	-9.3×10^{-4}	-0.0061	$1.8 \times \mathbf{10^{-5}}$	-0.0098
Rectified	-9.3×10^{-4}	-0.0061	$2.4 \times \mathbf{10^{-4}}$	-0.0099

TABLE II
COMPARISON OF COEFFICIENTS FOR VIRTUAL PLANE 4

	$\pi_4(1)$	$\pi_4(2)$	$\pi_4(3)$	$\pi_4(4)$
Original	-0.0130	-0.04	0.00084	-1.1685
Rectified	-0.0129	-0.04	0.0062	-1.1729

it is shown that c^e and $c^{e'}$ are not equal in general, unless $\pi_2^e = \pi_2$ and $\pi_4^e = \pi_4$. As a result, the depth difference Z_d of the two reconstructed points will be greater than zero with incorrect plane coefficients. Without loss of generality and considering the impact of noise, we conclude that the correct reconstruction result should have the least deformation in the z dimension. Thus, we propose the fundamental least deformation principle to rectify the errors of the plane equations. It contains the following two steps.

Step 1: Reconstruct a flat mirror surface with the proposed system. The flat mirror is placed at $z = 1$ mm in our experiment.

Step 2: Search and find the most accurate plane parameters $\pi_2(1), \pi_2(2), \pi_2(3), \pi_2(4), \pi_4(1), \pi_4(2), \pi_4(3), \pi_4(4)$ that make the depth difference Z_d of the reconstructed mirror surface the least, which is formulated as follows:

$$Z_d = \max_{i=1\ldots N} Z_i^r - \min_{i=1,\ldots,N} Z_i^r \tag{48}$$

$$\hat{\theta} = \underset{\theta=\{\pi_2(1),\pi_2(2),\pi_2(3),\pi_2(4),\pi_4(1),\pi_4(2),\pi_4(3),\pi_4(4)\}}{\arg\min} (Z_d) \tag{49}$$

where Z_i^r is the ith z coordinate of the reconstructed surface, i is the index of the interception point, and N is the total number of the interception points. Then, replace the previous plane parameters with the new parameters from Step 2.

The comparison of original system parameters and the rectified system parameters after least deformation rectification are shown in and Tables I and II.

IV. EXPERIMENTAL SYSTEM

Fig. 2 shows the diagram of the closed-loop welding robot system, and Fig. 3 shows the practically established imaging and measurement system. Plane 2 is attached on the beam splitter to get better imaging quality due to the restriction of laser focus. The front surface of the beam splitter is placed at $y = -115$ mm, and the thickness of the beam splitter is 3 mm. Imaging plane 3 is placed at $y = -30$ mm. Two Dragonfly2 cameras synchronically record images on the two diffusive imaging planes at 60 frames/s. During system parameter calibration and computation, the laser rays are projected onto a horizontal screen, which is placed on the top of the Metric Lab Jack. As can be seen, the power of the laser rays is very limited compared with the arc light shown in Fig. 1. However, the arc light decays much more rapidly with distances than the reflected lasers. Hence, clear images can be acquired on the two diffusive planes with proper bandpass filters.

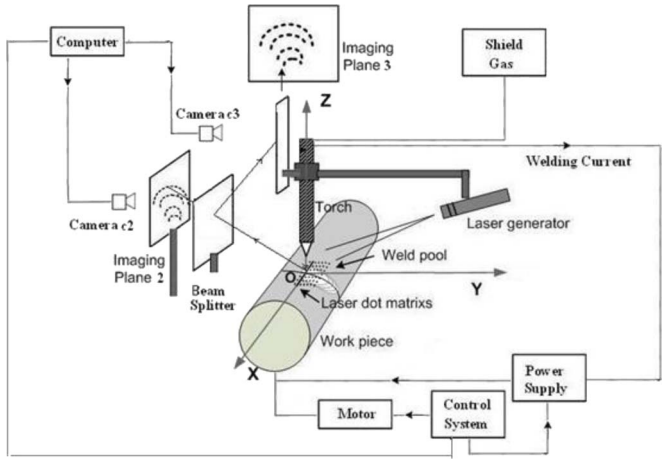

Fig. 2. Diagram of the closed-loop welding robot system.

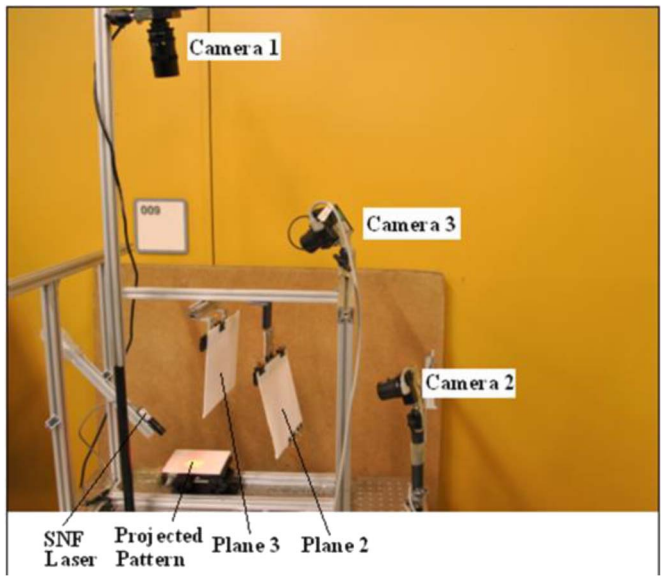

Fig. 3. Established imaging and measurement system.

During the welding process, the horizontal screen and the Metric Lab Jacks are replaced by a pipe, which is shown in Fig. 4(a). This pipe is a $4''$ schedule 10 stainless steel pipe, with an outside diameter of 114.3 mm (4.5 in) and a wall thickness of 3.1 mm (0.12 in), and is used as the workpiece for stationary gas tungsten arc welding. The used tungsten, which is fixed on the robotic arm as shown in Fig. 4(b), is 2% ceriated and its diameter is $3/32''$. The tip of the tungsten is shaped into a cone with a cone angle, and its distance to the workpiece is 6 mm. Pure argon is used as the shielding gas, and the flow rate is 8.5 l/min $(18ft^3/h)$. The welding power supply operates in the constant-current mode, and the current is 70 A. The angle of the center incident ray with the horizontal plane is 44°.

(a) (b)

Fig. 4. Part of the established welding system.

V. Results and Discussion

A. Experimental Results

To evaluate the reconstruction accuracy quantitatively, we reconstructed a flat mirror and compare the reconstruction accuracy with that of the previous work [36]. The reconstruction error is computed by the following:

$$\begin{bmatrix} E_x \\ E_y \\ E_z \end{bmatrix} = \begin{bmatrix} \frac{1}{N}\sum_{i=1}^{N}\left(X_r^i - X_o^i\right)^2 \\ \frac{1}{N}\sum_{i=1}^{N}\left(Y_r^i - Y_o^i\right)^2 \\ \frac{1}{N}\sum_{i=1}^{N}\left(Z_r^i - Z_o^i\right)^2 \end{bmatrix} \tag{50}$$

where E_x denotes the error in the x-direction, E_y denotes the error in the y-direction, and E_z denotes the error in the z-direction. (X_r^i, Y_r^i, Z_r^i) denotes the ith reconstructed point, and (X_o^i, Y_o^i, Z_o^i) denotes the ith original point. N denotes the total number of points.

The computed reconstruction error in the x-direction (E_x) is 0.30188 μm, the computed reconstruction error in the y-direction (E_y) is 0.59231 μm, and the computed reconstruction error in z-direction (E_z) is 2.3 μm. Compared with 20.7 μm (E_x) in the x-direction, 43.3 μm (E_y) in the y-direction, and 27.9 μm (E_z) in the z-direction in [36], the accuracy is increased significantly. The errors of the interpolated points are close to the average error of the points used to interpolate them because of the smoothness of the specular mirror.

Two weld pools at different times are reconstructed, and the results are shown in Figs. 5 and 6. From these results, the change of the weld pool shape during the welding process is vividly presented. The depth of the weld pool is about 0.4 mm at the starting stage $(T_1 = 1$ s) and then changes to about 0.8 mm after a while at $T_2 = 10$ s as shown in Fig. 5. In Fig. 6, it is seen that the depth of the weld pool becomes about 1 mm after 20 s, and the change of the shape becomes more rapidly. These measurement results are intended to be used as online feedback for the automated welding robot system to control the welding quality. In addition, they can also be used for the scientific study of the characteristics of weld pool. As can be seen, the depth and shapes of the weld pool change greatly with time, and the overall shape is irregular and convex.

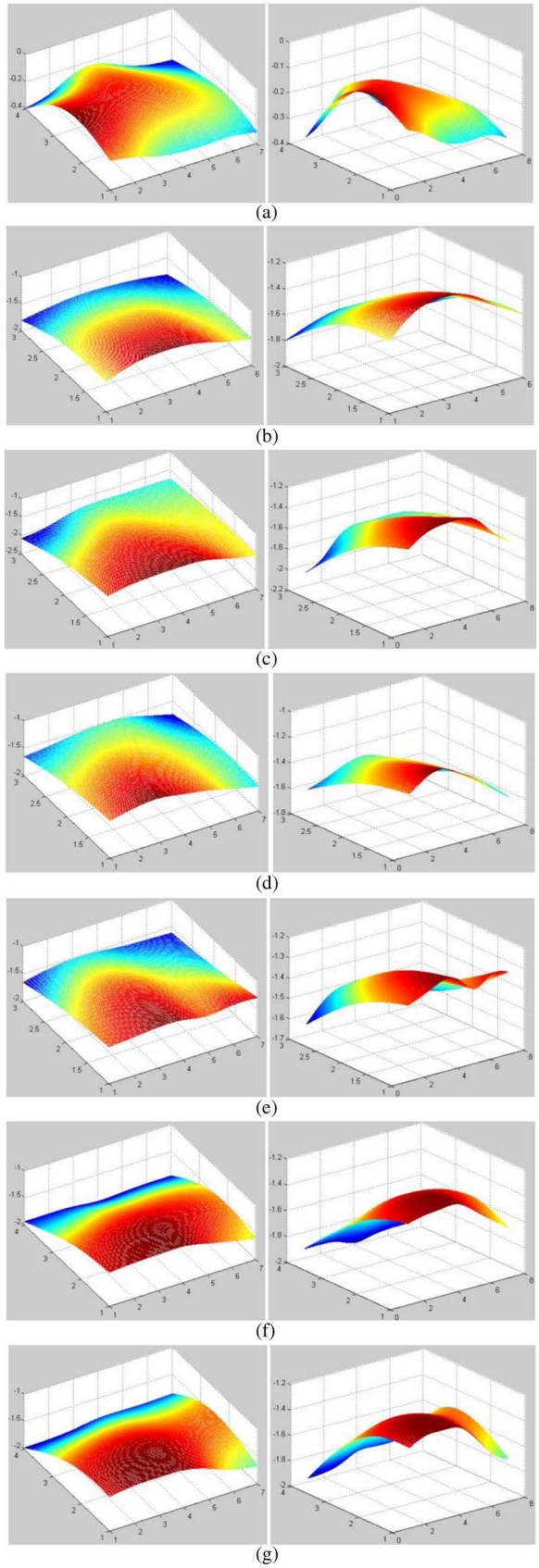

(a) (b) (c) (d) (e) (f) (g)

Fig. 5. Reconstruction results of weld pool 1 with two view angles at different times (the view angle of the right image is AZ $= 30$ and EL $= -60$, and the view angle of the right image is the default values AZ $= -37.5$, EL $= 30$). (a) $T_1 = 1$ s. (b) $T_2 = 10$ s. (c) $T_2 = 11$ s. (d) $T_4 = 12$ s. (e) $T_5 = 13$ s. (f) $T_6 = 14$ s. (g) $T_7 = 15$ s.

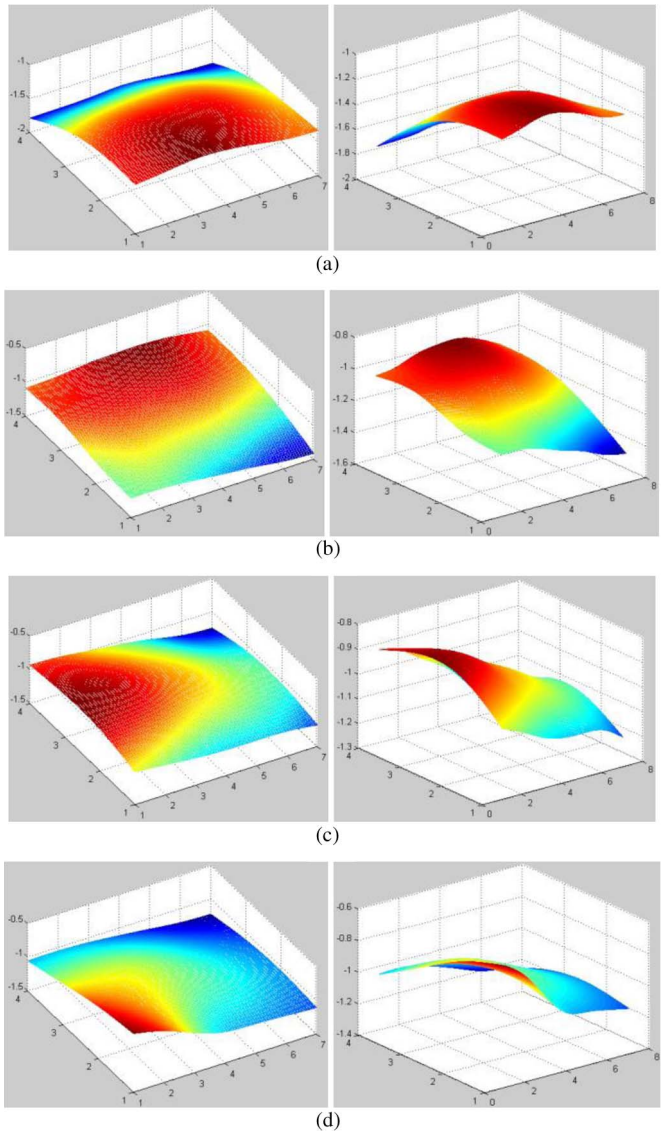

Fig. 6. Reconstruction results of weld pool 2 at different times with two view angles at different times (the view angle of the right image is AZ $=$ 30 and EL $=-60$, and the view angle of the right image is the default values AZ $=-37.5$ and EL $=30$). (a) $T_1 = 20$ s. (b) $T_2 = 21$ s. (c) $T_3 = 22$ s. (d) $T_4 = 23$ s.

B. Discussion

To demonstrate the superiority of the proposed method, we compared it with all the state-of-art literature that could be found and referenced. In addition to the quantitative results in [36], in [23], the average reconstruction error was reported to be 40 μm, which is worse than the results in this paper and those in [36].

We show the 3-D reconstructed weld pools of state-of-art methods in Figs. 7–13 for visual comparison with the results in this paper. Fig. 7 shows the reconstructed weld pool using the stereo method [28]. As shown, both image pairs are blurry, and it is difficult to find the corresponding matching points. Consequently, the reconstructed weld pool is not accurate with weird appearance. Fig. 8 shows the result from [26] where only the image pairs are shown in their paper. As shown, the image pairs are not better than those shown in Fig. 7(a). Consequently, their reconstructed weld pool is not accurate either. Fig. 9 shows the results from [22], which use an iterative computation

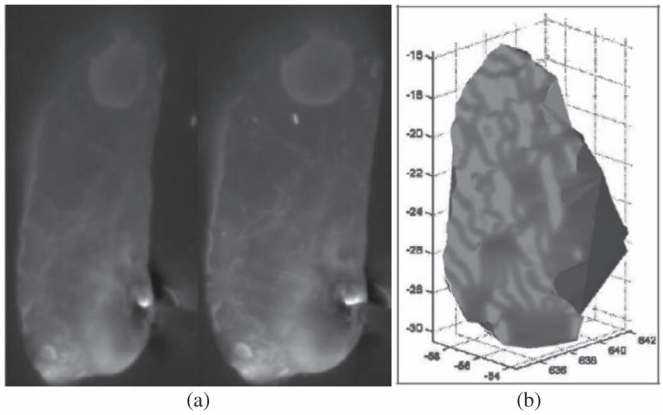

Fig. 7. Reconstruction results from [28].

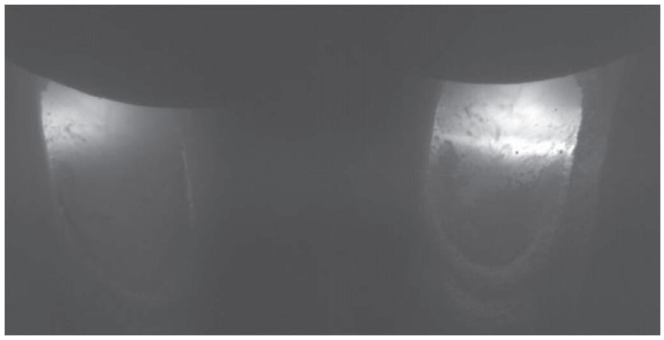

Fig. 8. Results from [26].

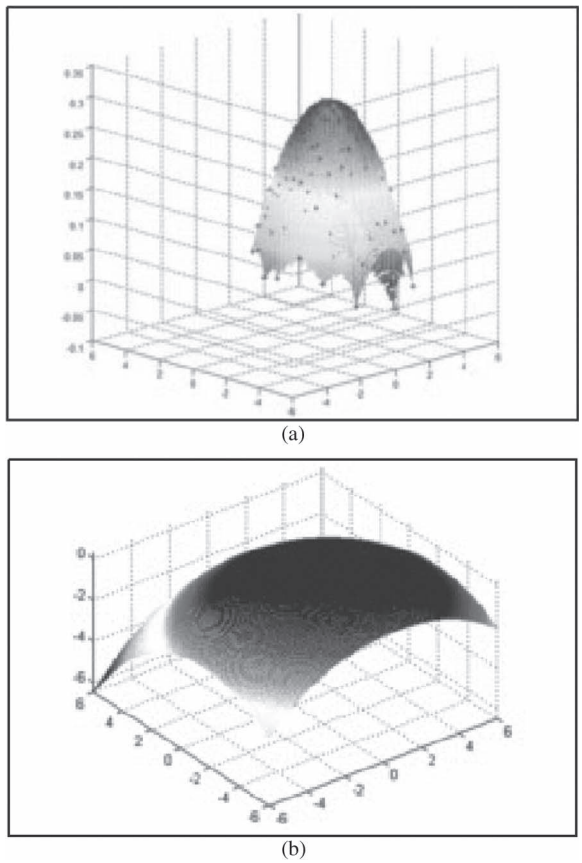

Fig. 9. Reconstructed weld pool from [22].

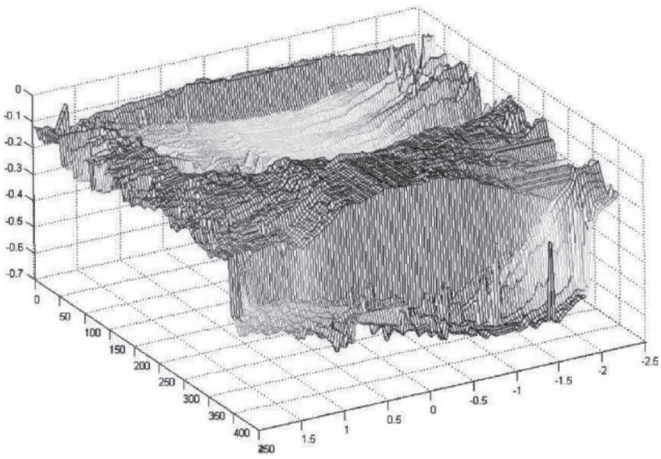

Fig. 10. Reconstructed weld pool from [19].

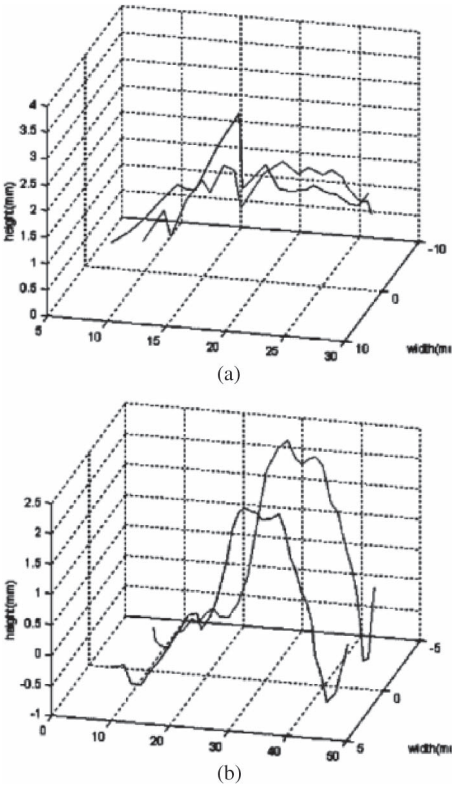

Fig. 11. Reconstructed weld pool from [27].

method for reconstruction. Fig. 9(a) shows the interpolation result, and Fig. 9(b) shows the extrapolation result, respectively. Both results are in symmetric shape, and extrapolation result is enormously enlarged. Thus, the reconstruction is inaccurate and unrealistic. Fig. 10 shows the reconstructed weld pool from [19], and it contains some reasonable information (e.g., the depth variation) about the weld pool; however, the result is too noisy and contradictory to the smooth weld pool surface. Thus, it also lacks accuracy. Fig. 11 shows the result from [27], where only some lines are shown. These lines did not reflect the depth of the weld pool correctly and enlarged it significantly. In addition, its resolution is too low to give a meaningful surface. The reconstructed weld pool from [23] is shown in Fig. 12, and it appears reasonable with a second-order polynomial assumption. Unfortunately, the assumption is not always true, and the

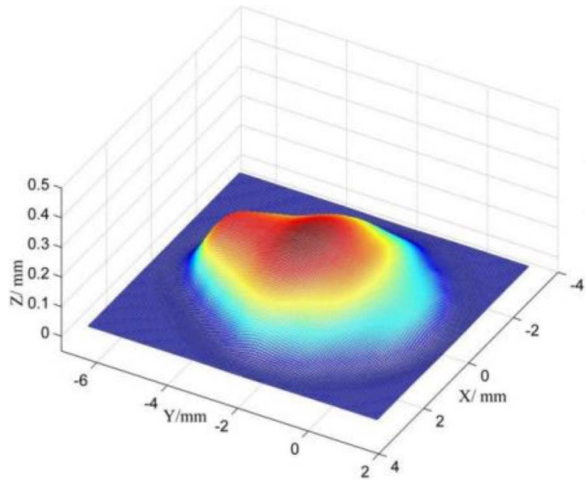

Fig. 12. Reconstructed weld pool from [23].

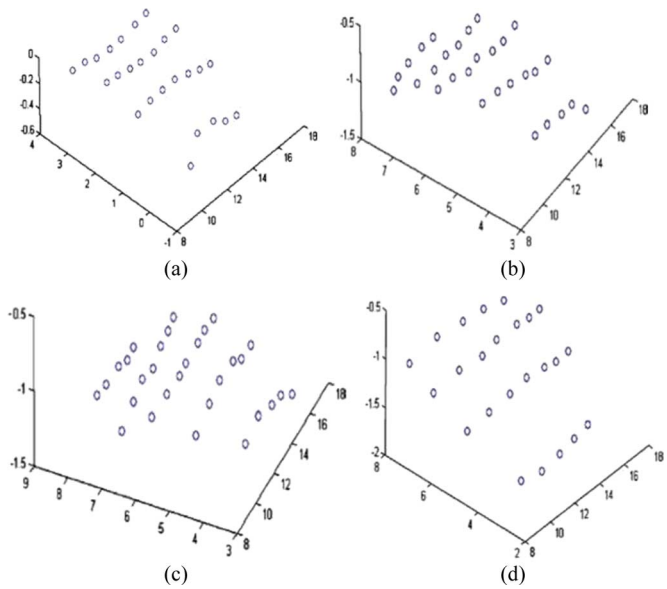

Fig. 13. Reconstructed weld pools from [38].

result is estimated instead of being accurately and analytically solved. Fig. 13 shows the reconstructed results from [38], and only some points are reconstructed. Its resolution is also too low to give a meaningful weld pool surface as [27], although its solution is analytical and accurate.

In [3], a mathematic model is developed to account for the convection and temperature distribution of a moving (dynamic) weld pool, and its validity can only be computed by the agreement of the observed fusion boundaries because of the lack of accurate 3-D shape information at that time. With accurately reconstructed 3-D weld pool sequences, it is more reliable for model validation as in [3]; thus, it becomes much easier for the scientific study of the physical characteristics of the weld pool and welding process.

Another major goal of this research is to use the measured weld pool as the feedback for the online control of the welding process. Hence, unsupervised image processing algorithms [42]–[62] to segment the laser points and register the two pairs of points robustly and efficiently become critical for this application, which will be addressed in our future research.

VI. Conclusion and Future Work

It is significant to measure the weld pool shape to provide feedback information for the automated welding robot system to control the welding quality. Through intercepting the reflection of a projected laser pattern twice, the proposed system gives a closed-form solution for each reflected ray and a closed-form solution for the corresponding intersection point on the weld pool surface. The weld pool shape can thus be reconstructed by one-shot structured light projection, which is capable of measuring dynamic specular surfaces in real time. The proposed least deformation principle rectifies the plane coefficient errors effectively and is fundamental for the practical implementation of the proposed system. Experimental results show that the proposed system is effective and robust in measuring the weld pool shapes. It is significantly better than other state-of-the-art methods both in robustness and efficiency.

The future work includes but not limited to the following: 1) establishing the quantitative relationship among weld pool shape and welding penetration; 2) measuring the weld pool shape for other welding process, e.g., gas metal arc welding.

References

[1] J. M. Wang, S. T. Wu, S. C. Yen, and H. J. Chiu, "A simple inverter for arc-welding machines with current doubler rectifier," *IEEE Trans. Ind. Electron.*, vol. 58, no. 11, pp. 5278–5281, Nov. 2011.

[2] G. S. Tzafestas and J. E. Kyriannakis, "Regulation of GMA weldingthermal characteristics via a hierarchical MIMO predictive control schemeassuring stability," *IEEE Trans. Ind. Electron.*, vol. 47, no. 3, pp. 668–678, Jun. 2000.

[3] S. Kou and Y. H. Wang, "Weld pool convection and its effects," *Welding J.*, vol. 65, no. 2, pp. 63-s–70-s, Mar. 1986.

[4] G. E. Cook, "Robotic arc welding: Research in sensory feedback control," *IEEE Trans. Ind. Electron.*, vol. 30, no. 3, pp. 252–268, Aug. 1983.

[5] C. Umeagukwu, B. Maqueira, and R. Lambert, "Robotic acoustic seam tracking: System development and application," *IEEE Trans. Ind. Electron.*, vol. 36, no. 3, pp. 223–229, Aug. 1989.

[6] C. Umeagukwu and J. Mccormick, "Investigation of an array technique for robotic seam tracking of weld joints," *IEEE Trans. Ind. Electron.*, vol. 38, no. 3, pp. 223–229, Jun. 1991.

[7] G. B. R. Andersen and K. Cook, "Synchronous weld pool oscillation for monitoring and control," *IEEE Trans. Ind. Appl.*, vol. 33, no. 2, pp. 464–471, Mar./Apr. 1997.

[8] R. Kovacevic, Y. Zhang, and S. Ruan, "Sensing andcontrol of weld pool geometry for automated GTA welding," *J. Manuf. Sci. Eng.*, vol. 117, no. 2, pp. 210–222, May 1995.

[9] Y. M. Zhang and L. Li, "Dynamic estimation of full penetration using geometry of adjacent weld pools," *J. Manuf. Sci. Eng.*, vol. 119, no. 4A, pp. 631–644, Nov. 1997.

[10] C. Fan, F. Lv, and S. Chen, "Visual sensing and penetration control in aluminum alloy pulsed gta welding," *Int. J. Adv. Manuf. Technol.*, vol. 42, no. 1, pp. 126–137, May 2009.

[11] A. N. Belbachir, M. Hofstätter, M. Litzenberger, and P. Schön, "High-speedembedded-object analysis using a dual-line timed-address-eventtemporal-contrast vision sensor," *IEEE Trans. Ind. Electron.*, vol. 58, no. 3, pp. 770–783, Mar. 2011.

[12] A. Kumar, "Computer-vision-based fabric defect detection: A survey," *IEEE Trans. Ind. Electron.*, vol. 55, no. 1, pp. 348–363, Jan. 2008.

[13] Z. Song and R. Chung, "An accurate and robust strip-edge-based structured light means for shiny surface micromeasurement in 3-D," *IEEE Trans. Ind. Electron.*, vol. 60, no. 3, pp. 1023–1032, Mar. 2013.

[14] Y. Q. Wei, N. S. Liu, X. Hu, and X. Ai, "Phase-correction algorithm of deformed grating images in the depth measurement of weld pool surface in gas tungsten arc welding," *Opt. Eng.*, vol. 50, no. 5, May 2011, Art. ID. 057209.

[15] C. Balfour, J. Smith, and A. Al-Shamma, "A novel edge feature correlation algorithm for real-time computer vision-based molten weld pool measurements," *Welding J.*, vol. 85, no. 1, pp. 1s–8s, Jan. 2006.

[16] N. Coniglio, A. Mathieu, O. Aubreton, and C. Stolz, "Characterizing weld pool surfaces from polarization state of thermal emissions," *Opt. Lett.*, vol. 38, no. 12, pp. 2086–2088, Jun. 2013.

[17] G. Saeed and Y. M. Zhang, "Mathematical formulation and simulation of specular reflection based measurement system for gas tungsten arc weld pool surface," *Meas. Sci. Technol.*, vol. 14, no. 8, pp. 1671–1682, Sep. 2003.

[18] G. Saeed, M. J. Lou, and Y. M. Zhang, "Computation of 3D weld pool surface from the slope field and point tracking of laser beams," *Meas. Sci. Technol.*, vol. 15, no. 2, pp. 389–403, Feb. 2004.

[19] G. Saeed, "Weld pool surface monitoring and depth extraction using a calibrated CCD sensor," in *Proc. Trends Welding Conf.*, Pine Mountain, GA, USA, May 16–20, 2005, pp. 665–670.

[20] A. C. Guu and S. I. Rokhlin, "Technique for simultaneous real-time measurements of welding pool surface geometry and arc force," *Welding J.*, vol. 71, no. 12, pp. 473s–482s, 1992.

[21] C. S. Wu, J. Q. Gao, X. F. Liu, and Y. H. Zhao, "Vision-based measurement of weld pool geometry in constant-current gas tungsten arc welding," in *Proc. Inst. Mech. Eng., J. Eng. Manuf.*, 2003, vol. 217, pp. 879–882.

[22] H. S. Song and Y. M. Zhang, "Measurement and analysis of three dimensional specular gas tungsten weld pool surface," *Welding J.*, vol. 87, no. 4, pp. 85s–95s, 2008.

[23] W. J. Zhang, X. W. Wang, and Y. M. Zhang, "Analytical real-time measurement of three-dimensional weld pool surface," *Meas. Sci. Technol.*, vol. 24, no. 11, Nov. 2013, Art. ID. 115011.

[24] W. J. Zhang, X. Zang, and Y. M. Zhang, "Robust pattern recognition for measurement of three dimensional weld pool surface in GTAW," *J. Intell. Manuf.*, DOI: 10.1007/s10845-013-0825-z, Aug. 2013.

[25] Y. D. Zhang, Z. M. Liang, D. L. Wang, and J. Wang, "3D Reconstruction of weld pool surface by a Biprism stereo system," *Appl. Mech. Mater.*, vol. 236/237, pp. 469–473, 2012.

[26] C. X. Zhao, I. M. Richardson, S. Kenjeres, C. R. Kleijn, and Z. Saldj, "A stereo vision method for tracking particle flow on the weld pool surface," *J. Appl. Phys.*, vol. 105, no. 12, Jun. 2009, Art. ID. 123104.

[27] G. Saeed, "Vision-based sensing of the welding process: A survey," *Int. J. Model., Identification Control*, vol. 1, no. 2, pp. 84–93, 2006.

[28] C. Mnich, F. Al-Bayat, C. Debrunner, J. Steele, and T. Vincent, "In situ weld pool measurement using stereovision," in *Proc. ASME Japan-USA Symp. Flexible Autom.*, Jul. 2004, pp. 1–2.

[29] D. H. Lee and I. Kweon, "A novel stereo camera system by a Biprism," *IEEE Trans. Robot. Autom.*, vol. 16, no. 5, pp. 528–541, Oct. 2000.

[30] K. N. Kutulakos and E. Steger, "A theory of refractive and reflective 3D shape by light-path triangulation," *Int. J. Comput. Vis.*, vol. 76, no. 1, pp. 13–29, Jan. 2008.

[31] Z. Z. Wang, "Robust measurement of the diffuse surface by phase shift profilometry," *J. Opt.*, vol. 16, no. 10, Oct. 2014, Art. ID 105407.

[32] L. C. Chen and X. L. Nguyen, "Dynamic surface profilometry and resonant mode detection for microstructure characterization using non-conventional stroboscopic interferometry," *IEEE Trans. Ind. Electron.*, vol. 57, no. 3, pp. 1120–1126, Mar. 2010.

[33] S. Y. Cho and W. S. Chow, "A neural-learning-based reflectance modelfor 3-D shape reconstruction," *IEEE Trans. Ind. Electron.*, vol. 47, no. 6, pp. 1346–1350, Dec. 2000.

[34] H. Cho and S. W. Kim, "Mobile robot localization using biased chirpspread-spectrum ranging," *IEEE Trans. Ind. Electron.*, vol. 57, no. 8, pp. 2826–2835, Aug. 2010.

[35] J. Huber and V. Graefe, "Motion stereo for mobile robots," *IEEE Trans. Ind. Electron.*, vol. 41, no. 4, pp. 378–383, Aug. 1994.

[36] Z. Z. Wang, X. Y. Huang, R. G. Yang, and Y. M. Zhang, "Measurement of mirror surfaces using specular reflection and analytical computation," *Mach. Vis. Appl.*, vol. 24, no. 2, pp. 289–304, Feb. 2013.

[37] Z. Z. Wang, R. G. Yang, and Y. M. Zhang, "Analytical measurement of mirror surfaces by single shot with united modeling of incident rays," *Meas. Sci. Technol.*, vol. 23, no. 12, Dec. 2012, Art. ID. 125404.

[38] Z. Z. Wang, R. G. Yang, and Y. M. Zhang, "Analytical reconstruction of three-dimensional weld pool surface in GTAW," *J. Manuf. Process.*, vol. 15, no. 1, pp. 34–40, Jan. 2013.

[39] F. Marino, P. De Ruvo, G. De Ruvo, M. Nitti, and E. Stella, "HiPER 3-D: An omnidirectional sensor for high precision environmental 3-D reconstruction," *IEEE Trans. Ind. Electron.*, vol. 59, no. 1, pp. 579–591, Jan. 2012.

[40] Z. Nemoto, H. Takemura, and H. Mizoguchi, "Development of small sized omni-directional laser range scanner and its application to 3D background difference," in *Proc. 33rd Annu. Conf. IEEE Ind. Electron. Soc.*, Taipei, Taiwan, Nov. 5–8, 2007, pp. 2284–2289.

[41] Z. Y. Zhang, "A flexible new technique for camera calibration," *IEEE Trans. Pattern Anal. Mach. Intell.*, vol. 22, no. 11, pp. 1330–1334, Nov. 2000.
[42] D. Mukherjee, Q. M. Wu, and T. M. Nguyen, "Gaussian mixture model with advanced distance measure based on support weights and histogram of gradients for background suppression," *IEEE Trans. Ind. Informat.*, vol. 10, no. 2, pp. 1086–1096, May 2014.
[43] R. C. Luo and C. L. Chun, "Multisensor fusion-based concurrent environment mapping and moving object detection for intelligent service robotics," *IEEE Trans. Ind. Electron.*, vol. 61, no. 8, pp. 4043–4051, Aug. 2014.
[44] S. C. Huang and B. H. Chen, "Automatic moving object extraction through a real-world variable-bandwidth network for traffic monitoring systems," *IEEE Trans. Ind. Electron.*, vol. 61, no. 4, pp. 2099–2112, Apr. 2014.
[45] Z. Z. Wang, "Monitoring of GMAW weld pool from the reflected laser lines for real time control," *IEEE Trans. Ind. Informat.*, vol. 10, no. 4, pp. 2073–2083, Nov. 2014.
[46] X. Zhang, W. Hu, S. Chen, and S. Maybank, "Graph enbedding based learning for robust object tracking," *IEEE Trans. Ind. Electron.*, vol. 61, no. 2, pp. 1072–1084, 2014.
[47] J. S. Hu, J. J. Wang, and D. M. Ho, "Design of sensing system and anticipative behavior for human following of mobile robots," *IEEE Trans. Ind. Electron*, vol. 61, no. 4, pp. 1916–1927, Apr. 2014.
[48] D. Tao, L. Jin, Y. Wang, and X. Li, "Rank preserving discriminant analysis for human behavior recognition on wireless sensor networks," *IEEE Trans Ind. Informat.*, vol. 10, no. 1, pp. 813–823, Feb. 2014.
[49] Z. Z. Wang and Y. M. Zhang, "Robust and automatic segmentation of a class of fuzzy edge images," *Int. J. Model., Identification Control*, vol. 12, no. 1/2, pp. 88–95, 2011.
[50] Z. Z. Wang and Y. M. Zhang, "Brightness based selection and edge detection based enhancement separation algorithm for low resolution metal transfer images," *IEEE Trans. Autom. Sci. Eng.*, vol. 6, no. 1, pp. 181–187, Jan. 2009.
[51] H. D. Cheng, Y. H. Chen, and Y. Sun, "A novel fuzzy entropy a proach to image enhancement and thresholding," *Signal Process.*, vol. 75, no. 3, pp. 277–301, Jun. 1999.
[52] S. K. Pal, R. A. King, and A. A. Hashim, "Automatic gray level thresholding through index of fuzziness and entropy," *Pattern Recognit. Lett.*, vol. 1, no. 3, pp. 141–146, Mar. 1983.
[53] H. D. Cheng and Y. H. Chen, "Fuzzy partition of two-dimensional histogram and its application to thresholding," *Pattern Recognit.*, vol. 32, no. 5, pp. 825–843, May 1999.
[54] A. K. C. Wong and P. K. Sahoo, "A gray-level thresholding selection method based on maximum entropy principle," *IEEE Trans. Syst. Man Cybern.*, vol. 19, no. 4, pp. 866–871, Jul./Aug. 1989.
[55] C. H. Li and C. K. Lee, "Minimum cross-entropy thresholding," *Pattern Recognit.*, vol. 26, no. 4, pp. 617–625, Apr. 1993.
[56] A. G. Shanbag, "Utilization of information measure as a means of image thresholding," *Comput. Vis. Graph. Image Process.*, vol. 56, no. 5, pp. 414–419, Sep. 1994.
[57] N. Otsu, "A threshold selection method from gray level histogram," *IEEE Trans. Syst. Man Cybern.*, vol. SMC-9, no. 1, pp. 62–66, Jan. 1979.
[58] Z. Z. Wang, "An one-shot-projection method for measurement of specular surfaces," *Opt Exp.*, vol. 23, no. 3, pp. 1912–1929, Feb. 2015.
[59] C. Y. Xu and J. L. Prince, "Snakes, shapes, gradient vector flow," *IEEE Trans. Image Process.*, vol. 7, no. 3, pp. 359–369, Mar. 1998.
[60] J. B. Shi and J. Malik, "Normalized cuts and image segmentation," *IEEE Trans. Pattern Anal. Mach. Intell.*, vol. 22, no. 8, pp. 888–905, Nov. 2000.
[61] B. Wang, X. Gao, D. Tao, and X. Li, "A nonlinear adaptive level set for image segmentation," *IEEE Trans. Cybern.*, vol. 44, no. 3, pp. 418–428, Mar. 2014.
[62] S. Arabe, X. Gao, and B. Wang, "A fast and robust level set method for image segmentation using fuzzy clustering and lattice boltzmann method," *IEEE Trans. Cybern.*, vol. 43, no. 3, pp. 910–920, Jun. 2013.

Zhenzhou Wang received the B.S. and M.S. degrees in information engineering from Tianjin University, Tianjin, China, in 2000 and 2003, respectively, and the Ph.D. degree from the University of Kentucky, Lexington, KY, USA, in 2007.

He was a Researcher and a Postdoctoral Scholar with the University of Kentucky until 2012. In 2013, he was selected in the "Hundred Talents Program" of the Chinese Academy of Sciences and has worked as a Research Fellow and a Professor with Shenyang Institute of Automation, Chinese Academy of Sciences, Shenyang, China. He also serves on the Review Panel of Experts for the National Natural Science Foundation of China. His research interests include signal/image processing, machine/computer vision, stereo vision, structured light scanning technology, robotics technology, etc.